Received: 12 December 2022 | Revised: 4 June 2023 | Accepted: 29 August 2023

DOI: 10.1002/pip.3740

RESEARCH ARTICLE

PROGRESS IN PHOTOVOLTAICS WILEY

Curing conditions for low-resistivity contacts on transparent conductive oxide layers for different solar cell applications

Katharina Gensowski[1] | Timo Freund[2] | Maximilian Much[1] | Kazuo Muramatsu[3] | Sebastian Tepner[1] | Florian Clement[1]

[1]Production Technology - Structuring and Metallization, Fraunhofer Institute for Solar Energy Systems, Freiburg im Breisgau, Germany

[2]NICE Solar Energy GmbH (former), Schwäbisch Hall, Germany

[3]Namics Corporation, Niigata City, Japan

Correspondence
Katharina Gensowski, Production Technology - Structuring and Metallization, Fraunhofer Institute for Solar Energy Systems, Heidenhofstraße 2, Freiburg im Breisgau 79110, Germany.
Email: katharina.gensowski@ise.fraunhofer.de

Funding information
German Federal Ministry for Economic Affairs and Energy, Grant/Award Numbers: 03EE1086A, 03EE1006C

Abstract

The Cu $(In_{1-x}Ga_x)Se_2$ (CIGS) solar cell technology is a potentially high-efficient approach with unique properties compared with silicon photovoltaic, like flexible lightweight substrates and different colored designs. So far, the full potential of the transparent conductive oxide layers has not been exploited yet as no front contacts are applied, resulting in significant losses from the cell-to-module level. In this study, Ag front contacts are applied by parallel dispensing onto indium tin oxide layers of silicon heterojunction substrates and CIGS substrates. Subsequently, a thermally curing process is carried out to form the conductive contacts. The curing conditions are varied between $200°C \geq T_c \geq 100°C$ combined with $20\ min \geq t_c \geq 1.5\ min$. The study aims to determine the curing parameters enabling low-resistivity contacts by using low-temperature curing Ag paste and ultralow-temperature curing Ag paste. The lateral electrode resistance and the contact resistivity of printed electrodes are measured. The results of simultaneous thermogravimetry-differential scanning calorimetry (pastes) and microstructure analysis of printed electrodes are used to explain the electrical parameters of the printed electrodes. In general, higher curing temperatures and longer curing durations encourage the sintering and densification process of the applied electrodes resulting in low-resistivity contacts. Contact resistivities below $\rho_{c,TLM} < 5\ m\Omega{\cdot}cm^2$ and lateral electrode resistance of $R_{lateral} \geq 17\ \Omega\ m^{-1}$ are obtained for different paste systems. However, optimal curing conditions of low-temperature curing pastes can cause thermal damage to the CIGS device. Therefore, ultralow-temperature curing pastes seem to be promising candidates for front contact metallization of CIGS substrates.

KEYWORDS
Ag pastes, CIGS, conductive electrodes, contact formation, curing process, dispensing, SHJ, solar cell metallization, thin-film photovoltaics

1 | INTRODUCTION

In recent years, different research groups and industry are continuously working toward improvements of the metallization of silicon heterojunction (SHJ) solar cells concerning low-resistivity contacts to transparent conductive oxide (TCO) layers and low silver consumptions.[1–3] The architecture of the SHJ technology is described in the literature.[4,5] The SHJ approach only allows low-temperature processes of up to $T_c < 250°C$ to form the contact between printed electrodes and the TCO layer to avoid degradation of the amorphous silicon layer.[3,6,7] Mainly curing temperatures in the range of $T_c \approx 200°C$ are reported for printed electrodes.[8–11] Pastes with such curing conditions on SHJ solar cells are usually called low-temperature curing pastes. These high-viscous paste formulations are generally made up of micrometer-sized and/or nanometer-sized metal particles, binder resins, organic solvents, and curing agents.[3,12] Typically, lateral electrode resistivity below $\rho_{lateral} \leq 15$ μΩ·cm have been achieved with those paste formulations.[7,13,14] On R&D level, low-temperature curing pastes are applied by flatbed screen printing,[6,15] rotary printing,[16] inkjet printing,[17] and dispensing technique.[18,19] Nevertheless, flatbed screen printing remains the common industrial technique to create printed contacts on silicon solar cells.[1] Widths of screen-printed Ag electrodes down to $w_f = 16$ μm have been achieved using special, knotless screens and low-temperature curing pastes.[6]

In addition, front contacts on thin-film Cu $(In_{1-x}Ga_x)Se_2$ (CIGS) modules are also composed of low-temperature curing pastes.[20–22] Here, the electrodes are also applied onto TCO layers and orientated perpendicular to the P1P2P3 interconnections. The architecture of this thin-film concept,[23,24] its unique features,[25] and its industrial manufacturing processes[26,27] are illustrated in the literature. It should be mentioned that front contacts on CIGS substrates are not as common as on silicon solar cells. Front contacts on CIGS substrates are much more of a potential solution to overcome the significant cell-to-module efficiency gap. Bermudez et al. have described this phenomenon, including potential optimization approaches.[28]

Gensowski et al. have demonstrated that front contacts obtain higher CIGS module performance outputs than nonmetallized CIGS modules. Besides, a front-side metallization enables lower dead area of the active module area due to the usage of wider cells. The electrodes are applied by flatbed screen printing and parallel dispensing.[23] Nevertheless, published results show the limitation of front contact metallization of CIGS modules. Nowadays, curing temperatures of $T_c \approx 200°C$ are used to obtain the contact formation between printed electrodes and TCO layers, especially indium tin oxide (ITO) layers.[10,20,23] However, the CIGS technology requires even lower temperature processes than SHJ solar cells to prevent thermal damage to the CdS/CIGS interface. Ultralow-temperature curing pastes seem to be a promising candidate that enables the contact formation in a temperature range of $130°C \geq T_c \geq 100°C$. Few studies have presented the application of ultralow-temperature Ag pastes on silicon–perovskite tandem solar cells by flatbed screen printing.[29,30] Pingel et al. have shown lateral electrode resistances of $R_{lateral} \approx 5\ \Omega\ cm^{-1}$ when applying $T_c = 130°C$ as the curing temperature.[29] Until now, the availability of paste formulations which reach low-resistivity contacts combined with very ultralow-temperature processes is severely limited.[31]

In this study, well-performing curing parameters for a low-temperature Ag paste as well as an ultralow-temperature curing Ag paste are investigated to form low-resistivity contacts to ITO layers. The curing temperature T_c is varied in the range of $200°C \geq T_c \geq 100°C$ and the curing time t_c of 20 min ≥ t_c ≥ 1.5 min. Both high-viscous suspensions are applied onto SHJ substrates and CIGS substrates by parallel dispensing. The lateral electrode resistance $R_{lateral}$ and the contact resistivity $\rho_{c,TLM}$ of the printed Ag electrodes are measured. The study goal is to define the potential curing parameter space which achieves low-resistivity contacts on ITO layers taking into account the temperature sensitivity of CIGS modules. Therefore, nonmetallized CIGS substrates are likewise treated by the same thermal processes to determine the modules' I-V parameters and identify the potential resulting thermal damages. Additionally, the Ag pastes are analyzed by simultaneous thermogravimetry-differential scanning calorimetry (TG-DSC), and the microstructure characterization of selected Ag electrodes is conducted by scanning electron microscopy (SEM).[32,33]

The parallel dispensing technique is an extrusion process for solar cell metallization. Here, highly filled suspensions are extruded through micrometer-sized nozzles which are arranged in parallel.[34,35] It is a contactless printing process; only the paste threads get in contact with the substrate. These electrodes are characterized by their homogeneity and high aspect ratio resulting in relatively high effective silver usage compared with screen-printed structures.[19] High-temperature curing pastes and low-temperature curing pastes have been successfully applied as front contacts on different solar cell applications by parallel dispensing.[10,18,23,36]

2 | MATERIALS AND METHODS

This study includes three different types of substrates and two Ag pastes in order to evaluate the thermal damages of CIGS substrates depending on the curing conditions or rather the contact formation of printed Ag electrode to ITO layers depending on the curing conditions. The different substrate materials are the following: (1) small-sized CIGS modules. The material stack Mo/CIGS/chemical bath deposition (CBD)-CdS/i-ZnO/ZnO:Al/ITO is coated onto 3 mm thick glass substrates (Figure 1A,B), and the P1P2P3 scribing lines are realized sequential during the material deposition steps. The glass substrates are 156 mm × 156 mm in size; here, the aperture area of the small-sized CIGS modules is $A_{aperture} = 157.30\ cm^2$. In this case, one CIGS module consists of 29 cells (cell width $w_c = 4.069$ mm). This type of substrate is further described in our previous studies.[20,23] (2) CIGS TLM substrates. The material layers are identical to the small-sized CIGS modules but have no P1P2P2 scribing lines. The different layers are entirely deposited onto the 3 mm thick glass substrates (Figure 1C). NICE Solar Energy GmbH has provided all CIGS substrates. (3) SHJ substrates. The SHJ precursors are a commercial product; here, the top layer is also an ITO layer.

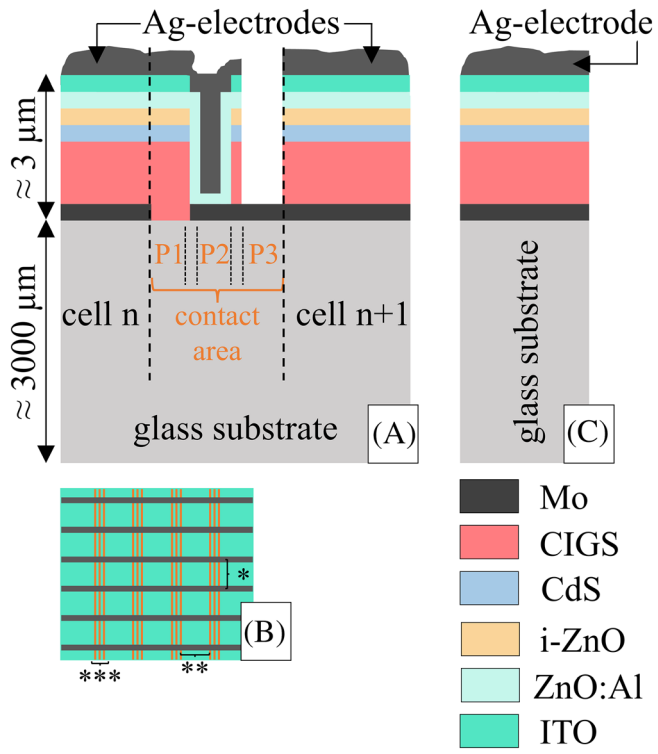

FIGURE 1 Cross-section sketch of a CIGS module. (A) The material stack Mo/CIGS/(CBD)-CdS/i-ZnO/ZnO:Al/ITO is deposited on a 3 mm thick glass substrate. Two cells are interconnected by P1P2P3 scribing lines. This contact area corresponds to a module's dead area. (B) Vertical alignment of P1P2P3 scribing lines and front electrodes (*electrode pitch; **cell width w_c; and ***P1P2P2 scribing lines). (C) CIGS TLM substrate. The material stack Mo/CIGS/(CBD)-CdS/i-ZnO/ZnO:Al/ITO is deposited on a 3 mm thick glass substrate.

In this case, a low-temperature curing Ag paste A[19,37] and an ultralow-temperature curing Ag paste B are applied onto those different substrate materials by parallel dispensing. Both paste formulations consist of an epoxy-phenolic resin system, solvents, and spherical Ag powders with varying particle sizes. Paste A is developed for the metallization of SHJ application, whereas paste B is developed for the metallization of perovskite application. The paste manufacturer recommends for paste A a curing temperature of $T_c = 200°C$ and for paste B a curing temperature of $T_c = 130°C$.

Experiment I examines the thermal damage of CIGS modules depending on the curing conditions. For that, substrate material (1) is used. The small-sized, nonmetallized CIGS modules are cured by using a continuous convection oven R0400FC from Essemtec AG (Switzerland). Curing temperatures of $200°C \geq T_c \geq 100°C$ in 10°C increments combined with curing times of $t_c = 1.5$, 5, 10, 15, and 20 min are applied to the samples. Three samples each are processed with the same curing combinations. In total, 165 samples are manufactured. Subsequently, contact strips are fixed to the heat-threaded CIGS modules to carry out the I-V measurements at standard test conditions. The samples are nonlaminated.

Experiment II investigates the contact formation between Ag electrodes to the ITO layers of the solar cell depending on the curing conditions. Here, especially the lateral electrode resistance $R_{lateral}$ and the contact resistivity $\rho_{c,TLM}$ are addressed. The lateral electrode resistance $R_{lateral}$ is defined in Equation (1), where $n_{electrode}$ is the number of electrodes, $R_{BB\text{-}BB}$ busbar-to-busbar grid resistance, and $d_{BB\text{-}BB}$ busbar-to-busbar distance.[38]

$$R_{lateral} = \frac{n_{electrode} \cdot R_{BB-BB}}{2d_{BB-BB}}. \quad (1)$$

The metal grids are applied onto the substrate materials (2) and (3) by parallel dispensing. The parallel dispensing process is conducted at a commercial table robot with our R&D print head.[39] Here, 10 nozzles are arranged in parallel on a nozzle plate. The electrode pitch is 1.556 mm. The low-temperature curing paste A is extruded through 35 µm nozzles and a process velocity of $v_{process|paste\ A} = 100\ mm\ s^{-1}$ is used. For the ultralow-temperature curing paste B, nozzle openings of D = 70 µm and a process velocity $v_{process|paste\ B} = 140\ mm\ s^{-1}$ are chosen. The dispensing gap is set to $d_{gap} = 500$ µm, which describes the distance between the nozzles of the print head and the substrate surface. Subsequently, the curing is performed as described for Experiment I.

The Ag electrodes are optically characterized by confocal laser scanning microscopy (CLSM) LEXT OLS 4000 from Olympus (Germany) and Schottky emission SEM.[32,40] The CLSM images are analyzed by a python™-based Fraunhofer internal software.[41] The samples for SEM characterization are prepared by Argon ion beam polishing to achieve smooth sample surfaces.[42] The SEM SU-70 from Hitachi (Japan) and Auriga 60 from Zeiss (Germany) with the InLens secondary electrons detector are used for characterizing the silver particle interconnections to each other or rather the silver particle connections to the ITO layer. In addition, the lateral electrode resistances of the Ag electrodes are measured by the industrial standard cell tester of Jonas & Redmann (Germany) using contact stripes. The contact resistivities $\rho_{c,TLM}$ are determined by the TLM Scan from pv-tools GmbH (Germany). To perform the transfer length method (TLM) measurements, the samples are cut in 10 mm stripes.[43,44]

Furthermore, both pastes are analyzed by simultaneous thermogravimetry-differential scanning calorimetry (TG-DSC) STA 449 F3 Jupiter® from Netzsch (Germany).[33,45] Approximately, 250 mg of paste is placed in an aluminum crucible. The heating rate is set to $10°C\ min^{-1}$ in a nitrogen atmosphere. Samples are heated from $T_{TG\text{-}DSC} = 20°C$ up to $T_{TG\text{-}DSC} = 100°C$, $T_{TG\text{-}DSC} = 150°C$, and $T_{TG\text{-}DSC} = 200°C$, and the final temperature is kept constant for $t_{TG\text{-}DSC} = 60$ min (isothermal plateau).

3 | RESULTS AND DISCUSSION

3.1 | Evaluation of suitable curing conditions for CIGS modules

Figure 2A shows the open-circuit voltage per cell V_{oc} and Figure 2B the maximum module point P_{mpp} of small-sized CIGS modules'

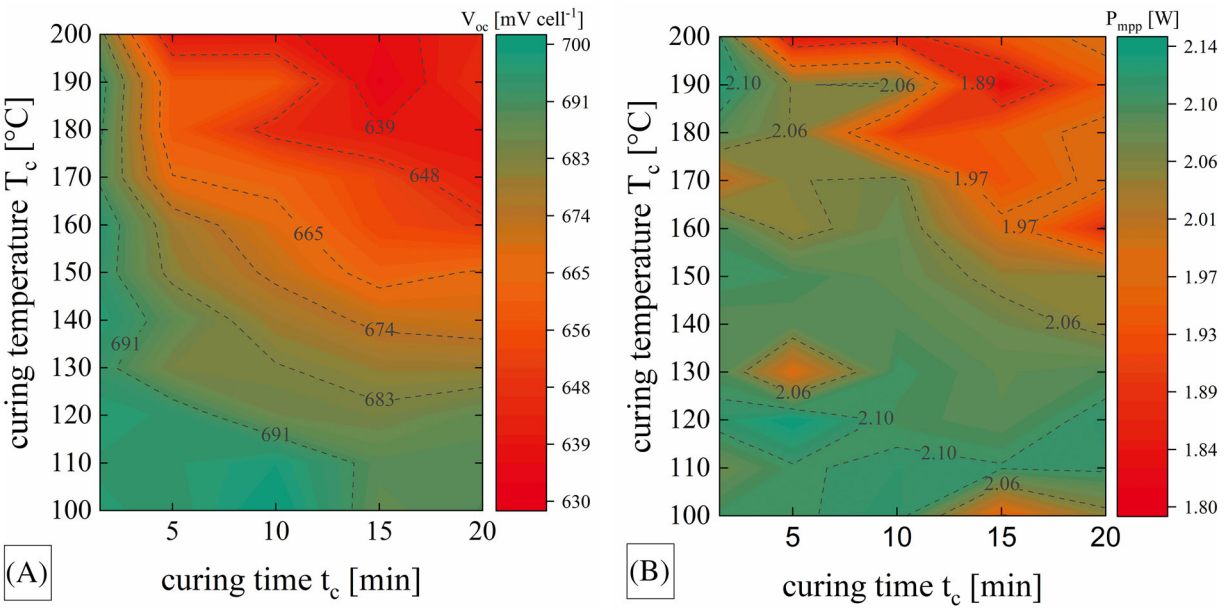

FIGURE 2 (A) Open-circuit voltage V_{oc} per cell and (B) maximum module point P_{mpp} of small-sized, nonlaminated CIGS modules depending on curing conditions measured by h.a.l.m. flasher I-V-tool at standard conditions. The mean value of three samples per curing parameter combination is mapped in the diagrams. The small-sized CIGS modules have aperture areas of $A_{aperture} = 157.30\ cm^2$ and cells with widths of $w_c = 4.069$ mm and are nonmetallized. The gray contour lines and values illustrate the open-circuit voltage per cell and the maximum module point, respectively.

dependency of the curing temperature T_c and curing time t_c. The CIGS modules are free of any front contacts. Here, the red coloring corresponds to a mean open-circuit voltage of $V_{oc} = 630$ mV cell^{-1} and the green coloring to a mean open-circuit voltage of $V_{oc} = 700$ mV cell^{-1} (Figure 2A). Curing temperatures of $T_c \leq 160°C$ combined with a short curing time of $t_c = 1.5$ min and curing temperatures of $T_c \leq 110°C$ combined with curing times of $t_c \leq 10$ min result in average open-circuit voltages of $V_{oc} \geq 691$ mV cell^{-1}. A gray-colored, dashed contour line visualizes this area in the plot. Small-sized CIGS modules have a mean open-circuit voltage of $V_{oc} = 639$ mV cell^{-1} when the curing process is conducted at $T_c = 200°C$ for $t_c = 5$ min and $T_c = 180°C$ for $t_c = 20$ min. The open-circuit voltage of small-sized CIGS modules is reduced either by relatively high curing temperatures in combination with already short curing durations or lower curing temperatures in combination with a relatively long curing duration. This open-circuit voltage drop may be caused by thermal damage in the CdS/CIGS interface. Further thermal damages in the CIGS layer itself may be possible as well.[20,22,23]

A decrease in open-circuit voltage may affect the module performance (Figure 2B). In this case, the red coloring of the color scale is equivalent to an average maximum power point of $P_{mpp} = 1.80$ W and the green coloring to a mean maximum power point of $P_{mpp} = 2.14$ W. An average open-circuit voltage of $V_{oc} = 698$ mV cell^{-1} results in a mean module performance of $P_{mpp} = 2.11$ W (curing parameters: $T_c = 110°C$ and $t_c = 10$ min). In comparison, a mean open-circuit voltage of $V_{oc} = 639$ mV cell^{-1} leads merely to a module performance of $P_{mpp} = 1.83$ W (curing parameters: $T_c = 200°C$ and $t_c = 5$ min). This decrease in module performance corresponds to a significant relative loss of $\Delta P_{mpp} = 15.30\%_{rel}$.

Based on this experimental data, curing conditions of below $T_c \leq 120°C$ combined with $t_c \leq 15$ min or $160°C \geq T_c \geq 130°C$ combined with $t_c \leq 5$ min are recommended when applying front contacts onto CIGS modules to prevent these losses in open-circuit voltage and, thus, in module performance. Furthermore, curing parameters of $150°C \geq T_c \geq 130°C$ combined with $t_c \leq 20$ min are suitable for contact formation; however, those conditions still have the risk of slight thermal damages and diffusion processes in the device.

3.2 | Required curing condition for low-resistivity contacts

Dispensed structures are uniform and homogenous along the entire electrode length and electrode height. A high optical aspect ratio is also characteristic for those structures.[36,46] Figure 3 presents two dispensed Ag electrodes printed with low-temperature curing Ag paste A (Figure 3A,B) and ultralow-temperature curing Ag paste B (Figure 3C,D). The low-temperature curing paste A and a curing process of $T_c = 200°C$ for $t_c = 20$ min form a low-resistivity contact to the ITO layer of SHJ substrate. The ultralow-temperature curing paste B enables a low-resistivity contact to the ITO layer of SHJ substrate, for example, when applying a curing temperature $T_c = 150°C$ for $t_c = 10$ min. Both contacts consist of cavities and voids, sintered as well as separated silver particles and organics, especially polymers. The contact zone itself shows silver particles with sintering bonds to the ITO layer and polymers that stick single silver particles to the ITO layer. The silicon pyramids are not fully covered with silver particles as gaps are present. The state of the particles and the amount of

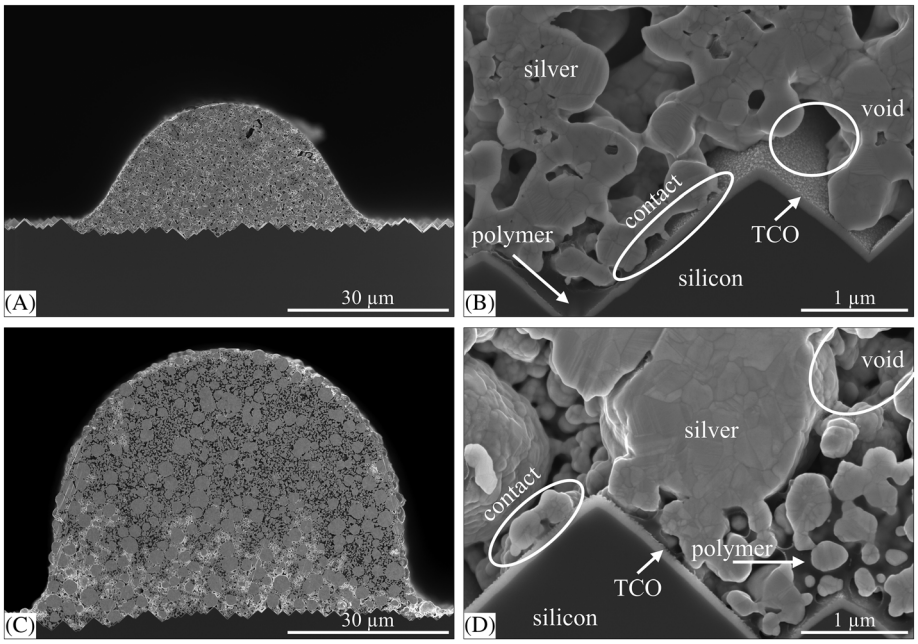

FIGURE 3 SEM images of dispensed Ag electrodes on SHJ substrate using InLens secondary electrons detector. (A) Electrode is printed with low-temperature curing Ag paste and then cured at curing temperature of $T_c = 200°C$ for $t_c = 20$ min (magnification of 1.5k×). (B) Silver particles of low-temperature Ag paste are sintered between each other and have formed a contact zone to the ITO layer (magnification of 30k×). (C) Electrode is printed with ultralow-temperature curing Ag paste and subsequently cured at curing temperature of $T_c = 150°C$ for $t_c = 10$ min (magnification of 1.5k×). (D) Silver particles of ultralow-temperature curing Ag paste are sintered between each other and are stuck to the ITO layer (magnification of 30k×).

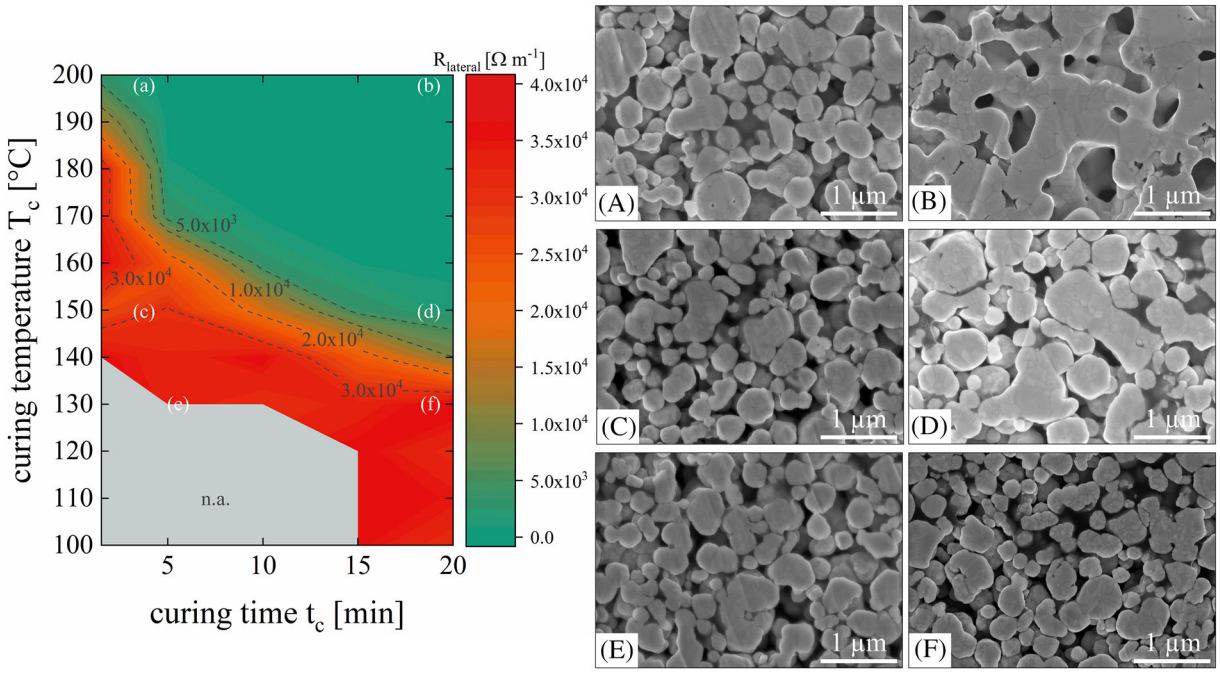

FIGURE 4 Lateral electrode resistance $R_{lateral}$ as a function of curing temperature T_c and curing time t_c of dispensed electrodes (left) and corresponding cross-section SEM images of those structures (magnification of 30k×) (right). The low-temperature curing Ag paste A is applied on SHJ substrates by parallel dispensing. Then, the contact formation process is conducted by varying the curing conditions. (A) $T_c = 200°C$ and $t_c = 1.5$ min; (B) $T_c = 200°C$ and $t_c = 20$ min; (C) $T_c = 150°C$ and $t_c = 1.5$ min; (D) $T_c = 150°C$ and $t_c = 20$ min; (E) $T_c = 130°C$ and $t_c = 5$ min; and (F) $T_c = 130°C$ and $t_c = 20$ min.

organics in Ag electrodes depend strongly on the curing process conditions influencing the densification of the entire electrode. In general, it is well known that low-thermal processes of metal contacts lead to porous, voided structures compared with high-thermal processes of metal electrodes which achieve in compact, densified structures.[3,7]

In this contribution, Ag electrodes which are printed with low-temperature curing paste A by using 35 µm nozzles show a mean core electrode width of $w_{core|SHJ|paste\text{-}A} = (47 \pm 1)$ µm ($w_{shading|SHJ|paste\text{-}A} = (57 \pm 1)$ µm) when applied to SHJ substrates or rather a mean core width of $w_{core|CIGS|paste\text{-}A} = (50 \pm 1)$ µm ($w_{shading|CIGS|paste\text{-}A} = (62 \pm 1)$ µm) when applied to CIGS substrates. These Ag electrodes feature a mean optical aspect ratio of $AR_{o|SHJ|paste\text{-}A} = (0.43 \pm 0.04)$ and $AR_{o|CIGS|paste\text{-}A} = (0.34 \pm 0.03)$, respectively. The optical aspect ratio of an electrode is defined as the ratio of the maximal electrode height

$h_{f,max}$ to the shading electrode width $w_{shading}$. Generally, an electrode shape can be described by different geometrical parameters presented in the literature.[34,38] When extruding ultralow-temperature curing paste B through nozzle openings of D = 70 µm with a process velocity of $v_{process} = 140$ mm s^{-1}, the resulting core electrode width is $w_{core|SHJ|paste\text{-}B} = (66 \pm 4)$ µm ($w_{shading|SHJ|paste\text{-}B} = (81 \pm 5)$ µm) or rather $w_{core|CIGS|paste\text{-}B} = (74 \pm 4)$ µm ($w_{shading|CIGS|paste\text{-}B} = (97 \pm 7)$ µm). The mean optical aspect ratio of these structures is $AR_{o|SHJ|paste\text{-}B} = (0.61 \pm 0.07)$ or $AR_{o|CIGS|paste\text{-}B} = (0.49 \pm 0.09)$, respectively. However, in previous studies, we have demonstrated the potential of the dispensing process in terms of low silver consumption and narrow electrode widths beyond the results of the present publication.[19,37]

3.2.1 | Low-temperature curing paste A

The lateral electrode resistance $R_{lateral}$ as a function of the curing processes is presented in Figure 4 (left). The low-temperature curing paste A is printed onto SHJ precursors in this case. The color scale ranges from $R_{lateral} = 0.0\ \Omega\ m^{-1}$ (green) to $R_{lateral} = 4.0{\cdot}10^{4}\ \Omega\ m^{-1}$ (red). Data points that are not available are colored in gray, as the Ag electrodes are not abrasion-resistant after the curing process, and thus, the characterization methods cannot be carried out. It is evident that high curing temperatures above $T_c \geq 180°C$ combined with curing times at least of $t_c = 10$ min result in low-resistivity contacts of $R_{lateral} = 5.0{\cdot}10^{3}\ \Omega\ m^{-1}$. Dispensed Ag electrodes which are cured at $T_c = 200°C$ for $t_c = 1.5$ min have a lateral electrode resistance in the mean of $R_{lateral} = 3.0{\cdot}10^{3}\ \Omega\ m^{-1}$. In contrast, lateral electrode resistance of $R_{lateral} = 7.7{\cdot}10^{1}\ \Omega\ m^{-1}$ is determined for dispensed Ag electrodes combined with a curing process of $T_c = 200°C$ and $t_c = 20$ min.

The SEM images visualize the different states of silver particles after thermal processes, which explain the different lateral electrode resistances (Figure 4A,B). A curing temperature of $T_c = 200°C$ and curing time of $t_c = 20$ min enable significant sintering of single silver particles and thus densification of electrodes. Therefore, the total surface area in the system decreases and the particle contact area increases by forming sinter necks. Such densification enhances the electrical conductivity of electrodes drastically. To cure Ag electrodes at $T_c = 200°C$ and $t_c = 1.5$ min will leave the silver particles separately to each other and the proportion of organics seems to be higher than for $t_c = 20$ min. Single sintering bonds between silver particles can be observed, especially starting from tiny particles due to melting point depression.[47,48] Both Ag electrodes contain voids, cavities, and gaps. Such porous structures printed with low-temperature curing pastes are typical, as shown in many studies. Schube presented that these cavities and gaps especially occur at silver/TCO interfaces due to the higher affinity of silver/silver interface sintering. Further, these voids may be caused by evaporation of solvents and polymerization processes.[7] Greer et al. and Pokluda et al. described the sintering processes of nanometer-sized particles in great detail.[49,50]

In addition, it is evident that curing temperatures below $T_c < 150°C$ lead to Ag electrodes with high lateral electrode resistances of $R_{lateral} \geq 3.0{\cdot}10^{4}\ \Omega\ m^{-1}$ or even not abrasion-resistant structures. Such high lateral electrode resistances indicate that the stabilizer shells (=capping layer on silver particles) have already been removed, allowing direct (point-like) particle–particle contacts with still low electrical conductivity. The SEM images illustrate that the silver particles have not formed sinter necks and individual silver particles are isolated in the organics at a relatively large distance to other particles. It seems that the organics of the low-temperature curing paste A have not resulted in any shrinkage and densification under these curing temperatures (Figure 4E,F).

The contact resistivity $\rho_{c,TLM}$ is measured by TLM measurements and is shown in Figure 5. Ag electrodes on ITO layers of SHJ solar cells show contact resistivities of $\rho_{c,TLM} \leq 3.6\ m\Omega{\cdot}cm^2$ for curing temperatures above $T_c \geq 180°C$ (Figure 5A). Curing temperatures below $T_c < 150°C$ enable no contact formation between the Ag electrode and the ITO layer of SHJ solar cells. To evaluate the impact of the ITO of SHJ substrates and CIGS substrates to the contact resistivities, a comparison of those substrates is shown in Figure 5B and Table 1. Here, the curing temperatures $200°C \geq T_c \geq 170°C$ are combined with a curing time of $t_c = 10$ min. All mean values for contact resistivities are smaller than $\rho_{c,TLM} \leq 5\ m\Omega{\cdot}cm^2$. Ag electrodes on CIGS substrates tend to have lower contact resistivities than Ag electrodes on SHJ substrates. For example, Ag electrodes onto an ITO of SHJ substrates show an average contact resistivity of $\rho_{c,TLM|SHJ} = (3.1 \pm 0.3)\ m\Omega{\cdot}cm^2$ and Ag electrodes onto an ITO of CIGS substrates have an average contact resistivity of $\rho_{c,TLM|CIGS} = (2.5 \pm 1.3)\ m\Omega{\cdot}cm^2$ (curing conditions: $T_c = 190°C$ and $t_c = 10$ min). The contact resistivities are similar to those presented in the literature.[20] The reference Ref. corresponds to dispensed Ag electrodes on CIGS substrates. In both studies, the same low-temperature curing paste was used for the parallel dispensing process achieving comparable electrode widths.[20] In addition, screen-printed and dispensed electrodes result in a comparable level of contact resistivity.[19,20] When interpreting the results of contact resistivities, the measurement inaccuracy of the TLM should be kept in mind.[51] Furthermore, it must be pointed out that the manufacturing process and the composition of the ITO layers have a distinct effect on the contact formation of the electrodes to that layer and consequently on the contact resistivity values, as described in the literature.[52,53]

The data allow the following observation: The lateral electrode resistance $R_{lateral}$ predicts if a contact between the Ag electrode and the ITO layer is formed or not. In this study, Ag electrodes which show lateral electrode resistances below $R_{lateral} \leq 5.0{\cdot}10^{3}\ \Omega\ m^{-1}$ form contact with contact resistivities below $\rho_{c,TLM} \leq 5.0\ m\Omega{\cdot}cm^2$.

To sum up the different results, shown in Figures 3–5, the performance index $I_{V\text{-}R}$ is introduced to quantify the trade-off between the thermal damages of CIGS modules and the lateral electrode resistance $R_{lateral}$ of printed structures (Equation 2). A performance index of $I_{V\text{-}R} = 100\%$ is equivalent to an open-circuit voltage of $V_{oc\text{-}limit|max} = 710\ mV\ cell^{-1}$ and a lateral electrode resistance of $R_{lateral\text{-}limit|min} = 10\ \Omega\ m^{-1}$ and is targeted. In contrast, an open-circuit voltage of $V_{oc\text{-}limit|min} = 610\ mV\ cell^{-1}$ and a lateral electrode resistance $R_{lateral\text{-}limit|max} = 40{,}000\ \Omega\ m^{-1}$ lead to the performance index of $I_{V\text{-}R} = 1\%$. These upper and lower limits of

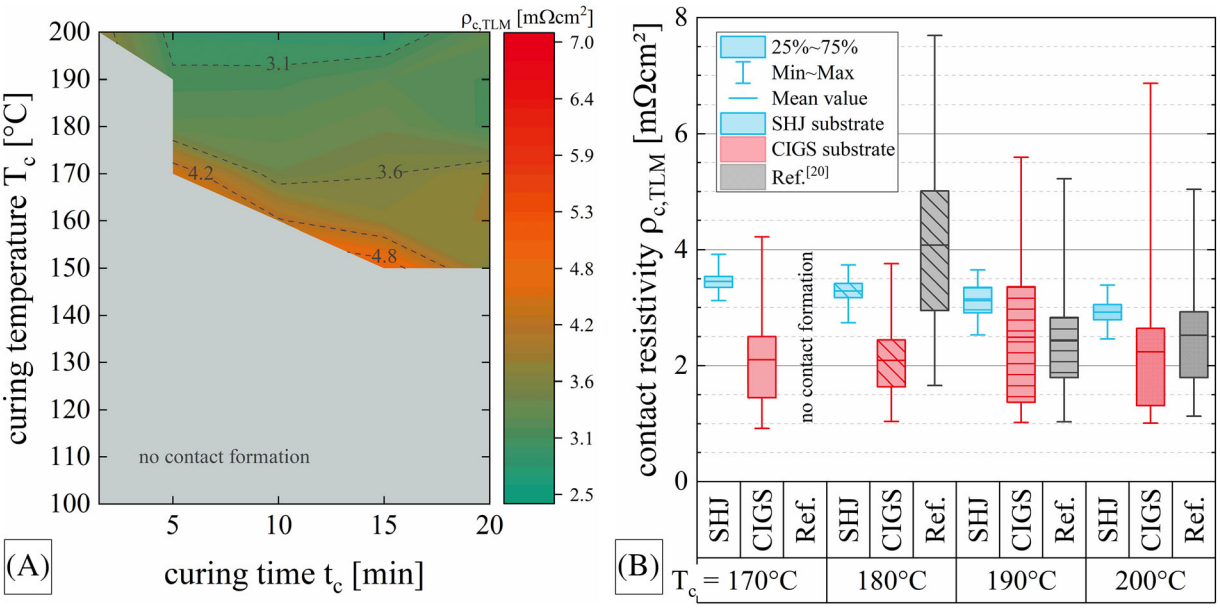

FIGURE 5 (A) Contact resistivity $\rho_{c,TLM}$ depending on curing temperature T_c and curing time t_c of dispensed electrodes (low-temperature curing paste A) on SHJ substrates and (B) SHJ and CIGS substrates. On the right, the curing temperatures T_c are combined with a curing time of $t_c = 10$ min. The reference refers to the contact resistivities $\rho_{c,TLM}$ shown in the literature.[20]

TABLE 1 Overview of mean contact resistivity $\rho_{c,TLM}$ depending on the curing temperature T_c combined with a curing time of $t_c = 10$ min and substrate (SHJ, CIGS, and Gensowski et al.[20]).

	Contact resistivity $\rho_{c,TLM}$ (mΩ·cm²)			
	$T_c = 170°C$	$T_c = 180°C$	$T_c = 190°C$	$T_c = 200°C$
SHJ	3.5 ± 0.2	3.3 ± 0.2	3.1 ± 0.3	2.9 ± 0.2
CIGS	2.1 ± 0.8	2.1 ± 0.6	2.5 ± 1.3	2.2 ± 1.3
Gensowski et al.[20]	–	4.1 ± 1.4	2.4 ± 0.9	2.5 ± 1.0

Note: The low-temperature curing paste A is used for the parallel dispensing tests.

lateral electrode resistance and open-circuit voltage are assumed. The weighting factors of the open-circuit voltage $v_{V\text{-}oc}$ and lateral electrode resistance $v_{R\text{-}lateral}$ are defined in Equations (3) and (5).

$$I_{V-R} = 0.5 \cdot v_{V-oc} + 0.5 \cdot v_{R-lateral}, \quad (2)$$

$$v_{V-oc} = 1 - \left(\left(V_{oc-limit|max} - V_{oc} \right) \cdot k_1 \cdot 100 \right), \quad (3)$$

$$k_1 = \frac{0.9}{\left(\left(V_{oc-limit|max} - V_{oc-limit|min} \right) \cdot 100 \right)}, \quad (4)$$

$$v_{R-lateral} = \left(\left(R_{lateral-limit|max} - R_{lateral} \right) \cdot k_2 \right) + 0.1, \quad (5)$$

$$k_2 = \frac{0.9}{\left(R_{lateral-limit|max} - R_{lateral-limit|min} \right)}. \quad (6)$$

The performance index $I_{V\text{-}R}$ varies in the range of $I_{V\text{-}R} = 44.70\%$ and $I_{V\text{-}R} = 85.74\%$ for the low-temperature curing paste A (Figure 6). The trade-off of open-circuit voltage losses and electrical conductivity losses of printed structures is within the gray-colored dash contour lines of $I_{V\text{-}R} = 71.13\%$ and hence corresponds to a range of different curing condition combinations. For instance, curing conditions of $T_c = 200°C$ and $t_c \leq 5$ min or $T_c = 150°C$ and $t_c \geq 15$ min allow a performance index of $I_{V\text{-}R} \geq 71.13\%$. Thus, the combination of higher curing temperatures T_c and short curing times t_c causes a similar performance index as lower curing temperatures T_c and longer curing times t_c within the range of the gray-colored, dashed contour lines of $I_{V\text{-}R} = 71.13\%$. The performance index $I_{V\text{-}R} = 85.74\%$ is achieved using a curing temperature of $T_c = 200°C$ and a curing time of $t_c = 1.5$ min for low-temperature curing paste A. However, a well-performing CIGS module requires low-resistivity contacts to the ITO layer. Following this, the white-colored, dotted line should be considered when choosing curing conditions for printed metal grids of low-temperature curing paste A.

In addition, the thermal analysis of the low-temperature curing Ag paste A provides explanations of the curing behavior of the paste and thus of the electrical properties of the printed structures. The data of the TG-DSC measurements are plotted over time in Figure 7. Here, three temperatures $T_{TG\text{-}DSC}$ are chosen as isotherms at $T_{TG\text{-}DSC} = 100°C$ (dotted line), $T_{TG\text{-}DSC} = 150°C$ (dashed line), and

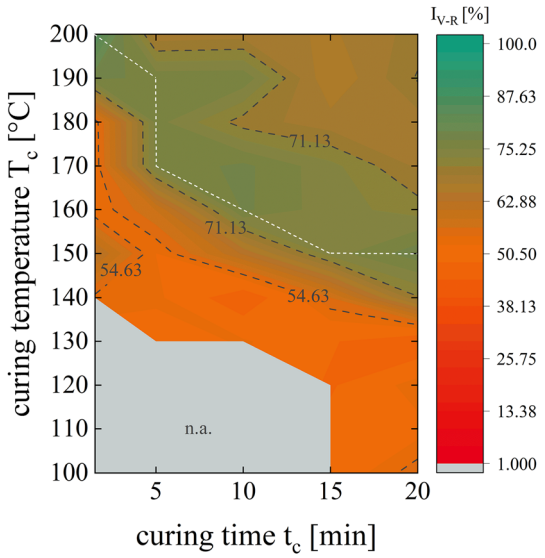

FIGURE 6 Performance index I_{V-R} as a function of curing temperature T_c and curing time t_c (low-temperature curing paste A). The performance index I_{V-R} values the compromise between thermal damages of CIGS cells ($\rightarrow V_{oc}$) and lateral electrode resistance $R_{lateral}$ of printed structures. The gray contour lines and values illustrate the performance index I_{V-R}. The white-colored dotted line visualizes the threshold to form a contact between the printed electrode and ITO layer ($\rightarrow \rho_{c,TLM}$).

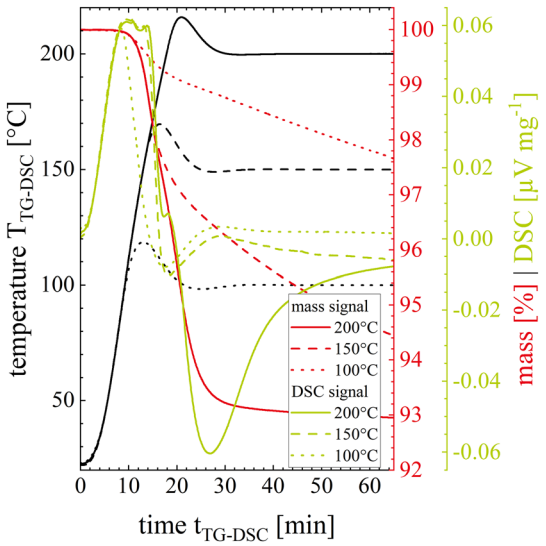

FIGURE 7 Thermal behavior of low-temperature curing Ag paste A. TG-DSC data over time for isotherms of $T_{TG-DSC} = 100°C$ (dotted line), $T_{TG-DSC} = 150°C$ (dashed line), and $T_{TG-DSC} = 200°C$ (complete line).

$T_{TG-DSC} = 200°C$ (complete line). It is obvious that the three TG curves show a significant drop over the measuring time t_{TG-DSC} where the relative losses in mass differ significantly. This drop indicates the evaporation of solvents as described in the literature.[8,54] The isothermal states at $T_{TG-DSC} = 100°C$ and $T_{TG-DSC} = 150°C$ cause significant losses in mass within the constant temperature range of $\Delta m_{100°C} = -1.5\%$ and $\Delta m_{150°C} = -2.5\%$, respectively. In contrast, the isothermal state at $T_{TG-DSC} = 200°C$ results in slight losses in mass within the constant temperature range of $\Delta m_{200°C} = -0.4\%$. Consequently, most of the proportion of the solvent is already evaporated before reaching the isothermal state at $T_{TG-DSC} = 200°C$ and only a few residuals volatilize. It seems that the low-temperature curing paste A consists of 93% of nonvolatile materials. The SEM image shows densified and sintered particles when using a curing temperature of $T_c = 200°C$ (Figure 4). It is presumed that the binder resin of the paste is not burned within the chosen temperature range as the TG curve does not show a second drop. Schube et al. noticed such a second drop at $T_{TG-DSC} = 284°C$ for a different low-temperature curing paste.[8]

Oh et al. investigated a low-temperature curing polymer Ag paste by thermogravimetric analysis and categorized the TG curve into three sections (I: slow response, II: rapid response, and III: saturated response).[9] These categories can also be established in the TG curve with an isothermal plateau at $T_{TG-DSC} = 200°C$; here, category II of rapid response begins at $T_{TG-DSC} = 155°C$. Besides the evaporation of solvents, the binder reacts, and the sintering process of particles is initiated. This thermal behavior of low-temperature curing paste A concedes with the electrical parameters of those printed Ag electrodes. It explains why no contact formation of the printed electrodes to the ITO layer below curing temperature $T_c < 150°C$ occurs. The proportion of volatile materials is too high, and the level of the sintering process of the silver particles is too low. It should be noted that the duration of the curing process itself is not represented in the TG-DSC, except in the isothermal states.

3.2.2 | Ultralow-temperature curing paste B

Figure 8 presents the lateral electrode resistance dependency on the curing processes. The electrode lateral electrode resistance is illustrated through the color scale which ranges from $R_{lateral} = 0.0\ \Omega\ m^{-1}$ (green) to $R_{lateral} = 4.0{\cdot}10^4\ \Omega\ m^{-1}$ (red). The majority of the experimental parameter space of this study enables lateral electrode resistances below $R_{lateral} \leq 8.3{\cdot}10^2\ \Omega\ m^{-1}$. More precisely, most curing parameters enable lateral electrode resistances in the range of $1.00{\cdot}10^2\ \Omega\ m^{-1} \geq R_{lateral} \geq 1.73{\cdot}10^1\ \Omega\ m^{-1}$. The SEM images show that the ultralow-temperature curing Ag paste B consists of two different Ag powders with different average particle sizes. Especially, those small silver particles are sintered to each other and the individual particle shape is no longer evident. These small silver particles are positively linked to bigger silver particles and thus cause more densified structures. The organics of the paste formulations are not uniformly distributed over the entire cross-sectional area of the Ag electrode; the organics are more arbitrary localized (Figure 3B). Also, in this case, higher curing temperatures lead to stronger sintering of

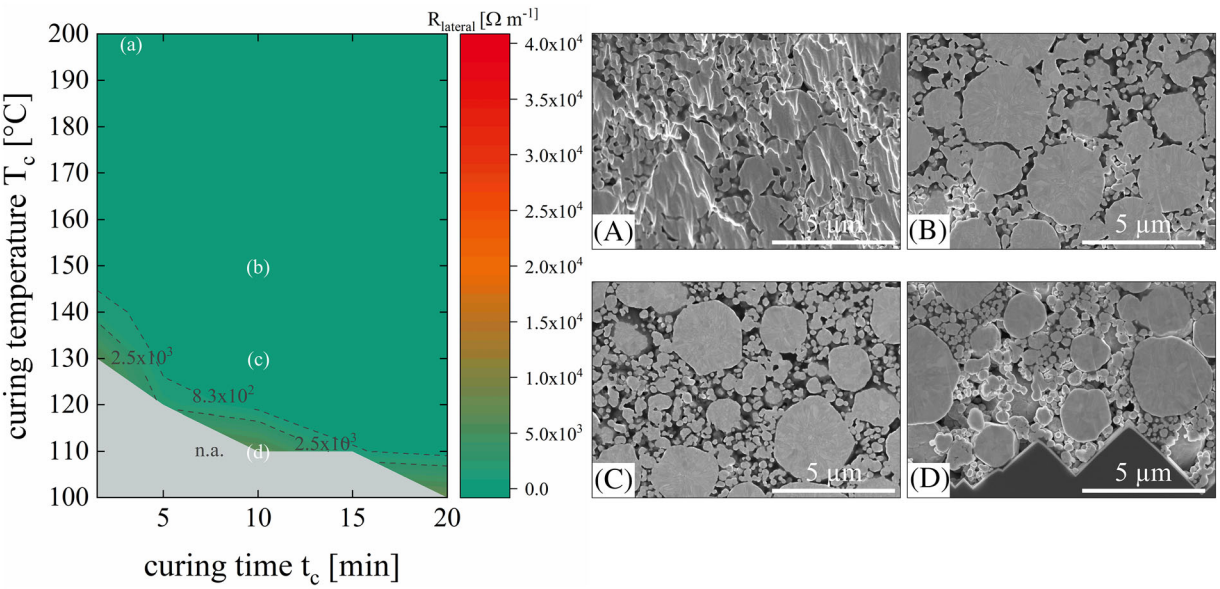

FIGURE 8 Lateral electrode resistance $R_{lateral}$ as a function of curing temperature T_c and curing time t_c of dispensed electrodes (left) and corresponding cross-section SEM images of those structures (magnification of 10k×) (right). An ultralow-temperature curing Ag paste B is applied onto SHJ substrates by parallel dispensing. Subsequently, a thermal process is conducted by using different curing parameters. (A) $T_c = 200°C$ and $t_c = 1.5$ min; (B) $T_c = 150°C$ and $t_c = 10$ min; (C) $T_c = 130°C$ and $t_c = 10$ min; and (D) $T_c = 110°C$ and $t_c = 10$ min.

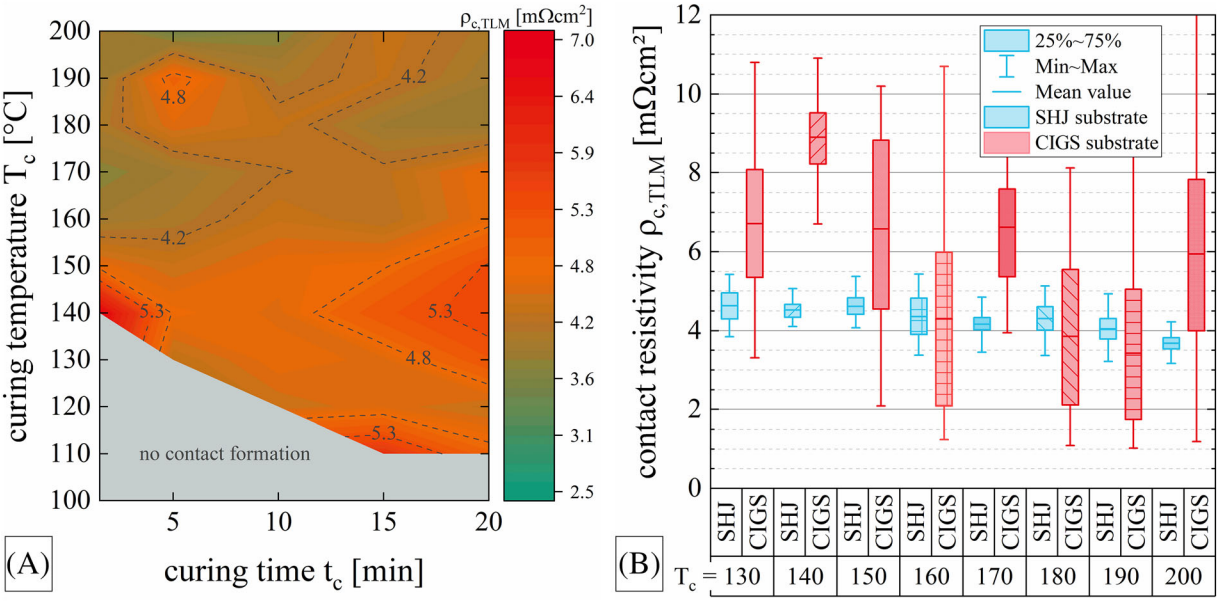

FIGURE 9 (A) Contact resistivity $\rho_{c,TLM}$ depending on curing temperature T_c and curing time t_c of dispensed electrodes (ultralow-temperature curing paste A) onto SHJ substrates and (B) onto SHJ and CIGS substrates. The contact formation processes are performed for $t_c = 10$ min.

single particles and densification. Curing temperatures below $T_c \leq 120°C$ are crucial to form electrically conductive Ag electrodes or even abrasion-resistant Ag electrodes on a substrate.

Ag electrodes which are printed with the ultralow-temperature curing Ag paste B have mean contact resistivities below $\rho_{c,TLM} < 7.0$ mΩ·cm^2 (Figure 9A). Ag electrodes which are cured at curing temperatures of $T_c \leq 120°C$ do not form any contact to the ITO layer of the SHJ solar cell. Figure 9B and Table 2 compare the contact resistivity of Ag electrodes on ITO layers (SHJ substrate) and ITO layers (CIGS substrate). The Ag electrodes have similar contact resistivities independent of the curing temperatures of $200°C \geq T_c \geq 130°C$ at a curing time of $t_c = 10$ min. These contact

TABLE 2 Overview of mean contact resistivity $\rho_{c,TLM}$ depending on the curing temperature T_c combined with a curing time of $t_c = 10$ min and substrate (SHJ and CIGS substrates).

	Contact resistivity $\rho_{c,TLM}$ (mΩ·cm^2)				
	SHJ	CIGS		SHJ	CIGS
$T_c = 130°C$	4.6 ± 0.4	6.7 ± 1.7	$T_c = 170°C$	4.2 ± 0.2	6.6 ± 1.5
$T_c = 140°C$	4.5 ± 0.2	8.9 ± 0.8	$T_c = 180°C$	4.3 ± 0.4	3.9 ± 1.8
$T_c = 150°C$	4.6 ± 0.3	6.6 ± 2.3	$T_c = 190°C$	4.0 ± 0.4	3.4 ± 2.1
$T_c = 160°C$	4.4 ± 0.5	4.3 ± 2.7	$T_c = 200°C$	3.7 ± 0.2	5.9 ± 2.4

Note: The ultralow-temperature curing paste B is applied by parallel dispensing.

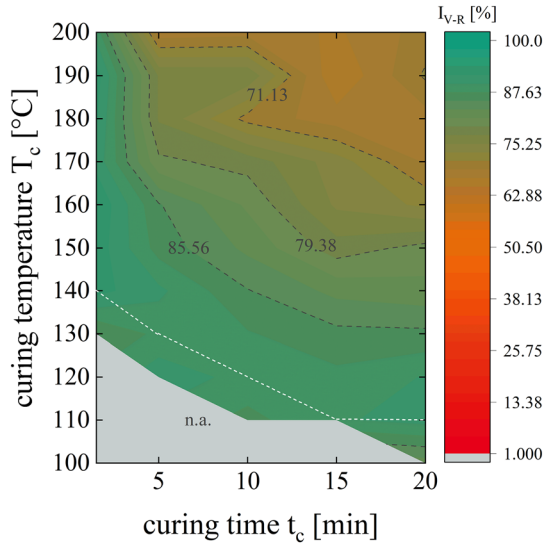

FIGURE 10 Performance index I_{V-R} depending on curing condition (ultralow-temperature curing paste B). The gray contour lines and values illustrate the performance index I_{V-R}. The white-colored, dotted line visualizes the threshold to form a contact between the printed electrode and ITO layer ($\rightarrow\rho_{c,TLM}$).

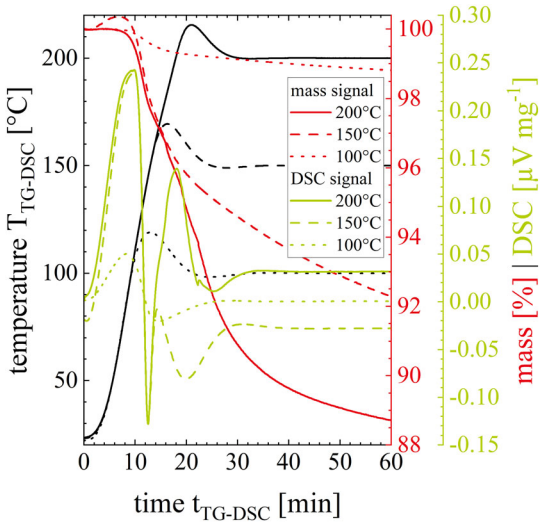

FIGURE 11 Thermal behavior of ultralow-temperature curing Ag paste B. TG-DSC data over time for isotherms of $T_{TG-DSC} = 100°C$ (dotted line), $T_{TG-DSC} = 150°C$ (dashed line), and $T_{TG-DSC} = 200°C$ (complete line).

resistivities range from $\rho_{c,TLM|200°C} = (3.7 \pm 0.2)$ mΩ·cm^2 to $\rho_{c,TLM|130°C} = (4.6 \pm 0.4)$ mΩ·cm^2 for Ag electrodes on ITO layers (SHJ substrates). The deviations within one experimental group are low, especially compared with Ag electrode on ITO layers of CIGS substrates. All Ag electrodes which are applied on ITO layers exhibit contact resistivities below $\rho_{c,TLM} \leq 10$ mΩ·cm^2. There is no clear tendency for the mean contact resistivity of Ag electrodes on CIGS substrates. Still, the contact resistivities tend to be higher than those on SHJ substrates. It should be mentioned that the sample preparation of CIGS substrates for TLM measurements was challenging as the Ag electrodes were quite brittle and poorly adhesive. Single Ag electrodes have come loose at the edges of the 10 mm stripes during the mechanical separation. It seems that curing temperatures above $T_c > 160°C$ minimize the structure adhesion of the electrodes to the ITO layers. Higher curing temperatures may cause negative effects on the ultralow-temperature curing Ag paste B.

The performance index I_{V-R} values the trade-off between the open-circuit voltage V_{oc} of CIGS cells and the lateral electrode resistance $R_{lateral}$ of printed contacts depending on the curing temperature T_c and the curing time t_c for ultralow-temperature curing paste B (Figure 10). Performance indexes between $I_{V-R} = 65.05\%$ and $I_{V-R} = 93.67\%$ are realized. In this case, curing parameters that are within the range of the gray-colored dash contour line of $I_{V-R} = 85.56\%$ and the white-colored dotted contour line are recommended. The performance index of $I_{V-R} = 93.67\%$ is obtained when using the curing temperature of $T_c = 160°C$ and the curing time of $t_c = 1.5$ min. This corresponds to a mean open-circuit voltage of $V_{oc} = 696$ mV cell^{-1} and a mean lateral electrode resistance of $R_{lateral} = 31.1\ \Omega\ m^{-1}$.

The achieved performance indexes of ultralow-temperature curing paste B also indicate that different curing parameters enable comparable performance index I_{V-R}, as already observed for low-temperature curing paste A. For example, combining the curing temperature $T_c = 190°C$ and the curing time $t_c = 5$ min results in a performance index of $I_{V-R} = 77.06\%$, whereas the curing temperature of $T_c = 150°C$ and the curing time $t_c = 15$ min enable the similar performance index of $I_{V-R} = 78.21\%$.

Figure 11 shows the thermal behavior of ultralow-temperature paste B up to an isothermal condition of $T_{TG\text{-}DSC} = 200°C$. The TG curve with the isothermal state of $T_{TG\text{-}DSC} = 100°C$ shows a loss in mass of $\Delta m_{100°C} = -1.2\%$ in total. Consequently, the printed structures are not abrasion-resistant because even the proportion of solvents is not fully evaporated. Heating the paste sample to $T_{TG\text{-}DSC} = 150°C$ causes a relative remaining mass of $m_{150°C} = 91.7\%$, following the evaporation of solvents has mostly occurred. In addition, the reactions of binders as well as the sintering process of particles proceed. This is supported by the electrical measurements of the printed structures and the SEM-based microstructure analysis. The SEM images of printed electrodes which are cured at $T_c = 150°C$ show sintered particles. At the end of the measurement, the TG curve with the isothermal state at $T_{TG\text{-}DSC} = 200°C$ shows a relative mass of $m_{200°C} = 88.3\%$ and it seems that the losses in mass would continue when carrying on with the measurement. Additionally, the DSC signal is at a positive level in the isothermal state at $T_{TG\text{-}DSC} = 200°C$. Both results allow the hypothesis that the thermal degradation of the binders and a further densification of the particles have started. This hypothesis could be strengthened by the weakening adhesion of the electrodes to the ITO layer and their more brittle appearance.

4 | CONCLUSION

In this work, a variation of curing temperatures and curing times of dispensed electrodes was conducted to specify the corresponding lateral electrode resistances and contact resistivities to ITO layers. First, a low-temperature curing Ag paste as well as an ultralow-temperature curing Ag paste was applied by parallel dispensing onto ITO layers of SHJ and CIGS substrates. Following this, a microstructure analysis of printed electrodes was performed by SEM. The goal was to define the curing conditions which enable low-resistivity contacts to the ITO layer, while considering the temperature sensitivity of CIGS modules.

The used CIGS modules allow thermal processes for front contact formation of $T_c \leq 160°C$ combined with $t_c \leq 5$ min without thermal damage to the device. Curing conditions of $T_c \leq 200°C$ and $t_c < 5$ min are applicable under the risk of slight losses in the open-circuit voltage V_{oc}. Nevertheless, the low-temperature curing Ag paste A requires curing temperature of above $T_c \geq 170°C$ to form contacts of contact resistivities below $\rho_{c,TLM} < 5\ m\Omega{\cdot}cm^2$. However, these results show opposite trends in choosing the most suitable curing parameters for printed contacts of paste A on CIGS modules. Following this, the performance index $I_{V\text{-}R}$ is introduced to quantify the compromise between the thermal damages of CIGS modules and the lateral electrode resistance $R_{lateral}$. A performance index of $I_{V\text{-}R} = 100\%$ is targeted. Performance indexes from $I_{V\text{-}R|paste\text{-}A} = 44.70\%$ to $I_{V\text{-}R|paste\text{-}A} = 85.54\%$ are reached for low-temperature curing paste A. For example, the curing conditions of $T_c = 200°C$ and $t_c = 1.5$ min are recommended resulting in a performance index of $I_{V\text{-}R|paste\text{-}A} = 85.54\%$.

Furthermore, for the first time, parallel dispensing was used to apply an ultralow-temperature curing Ag paste for solar cell metallization. Ultralow-temperatures Ag pastes seem to be promising for front contacts onto CIGS modules as curing temperatures of $T_c = 130°C$ are sufficient to achieve lateral electrode resistance of $R_{lateral} \geq 32\ \Omega\ m^{-1}$. Various curing parameters enable high performance indexes when contacts are printed with ultralow-temperature curing paste B. The combination of $T_c = 160°C$ and $t_c = 1.5$ min is suitable, leading to an outstanding performance index of $I_{V\text{-}R|paste\text{-}B} = 93.67\%$. The performance index ranges from $I_{V\text{-}R|paste\text{-}B} = 65.05\%$ to $I_{V\text{-}R|paste\text{-}B} = 93.67\%$. In general, ultralow-temperature curing paste B allows higher performance indexes than low-temperature curing A, mainly due to low lateral electrode resistances $R_{lateral}$ at low curing temperatures within the scope of experimental parameters. However, the contact resistivities as well as the possibility for fine-line printing need to be further improved for ultralow-temperature pastes. Another application for this paste system could also be perovskite solar cells. Finally, the thermal behavior of each paste system determined by TG-DSC measurements supports the microstructure analysis results and the printed electrode's electrical parameters.

AUTHOR CONTRIBUTIONS

Katharina Gensowski: Conceptualization; investigation; data analysis; visualization; writing—original draft; writing—review and editing. **Timo Freund:** Conceptualization; investigation; writing—review and editing. **Maximilian Much:** Investigation; writing—review and editing. **Kazuo Muramatsu:** Writing—review and editing. **Sebastian Tepner:** Writing—review and editing; project administration; supervision. **Florian Clement:** Writing—review and editing; funding.

ACKNOWLEDGEMENTS

This work was supported by the German Federal Ministry for Economic Affairs and Energy within the research projects "Altura" under the contract number 03EE1006C and "PrEsto" under the contract number 03EE1086A. The authors would like to thank NICE Solar Energy GmbH for providing CIGS samples and for the characterization of small-sized CIGS modules. A special thanks go to Philipp Köder, Niccola Zancan, and Joachim Müller. Furthermore, the authors would like to thank Elisabeth Bujnoch for SEM sample preparation and Jutta Zielonka for SEM characterization at Fraunhofer ISE. The authors are responsible for the content. Open Access funding enabled and organized by Projekt DEAL.

DATA AVAILABILITY STATEMENT

The data that support the findings of this study are available from the corresponding author upon reasonable request.

ORCID

Katharina Gensowski https://orcid.org/0000-0002-7227-724X

REFERENCES

1. VDMA Photovoltaic Equipment. *International Technology Roadmap for Photovoltaic (ITRPV) 2021 Results: Thirteenth Edition*; 2022.
2. Chunduri SK, Schmela M. *Heterojunction Solar Technology. TAIYANG NEWS: All About Solar Power* 2022.

3. Zeng Y, Peng C-W, Hong W, et al. Review on metallization approaches for high-efficiency silicon heterojunction solar cells. *Trans Tianjin Univ*. 2022;28(5):358-373. doi:10.1007/s12209-022-00336-9
4. de Wolf S, Descoeudres A, Holman ZC, Ballif C. High-efficiency silicon heterojunction solar cells. *A Review Green*. 2012;2(1):7-24. doi:10.1515/green-2011-0018
5. Haschke J, Dupré O, Boccard M, Ballif C. Silicon heterojunction solar cells: recent technological development and practical aspects—from lab to industry. *Sol Energy Mater Sol Cells*. 2018;187:140-153. doi:10.1016/j.solmat.2018.07.018
6. Descoeudres A, Allebé C, Badel N, et al. Low-temperature processes for passivation and metallization of high-efficiency crystalline silicon solar cells. *Sol Energy*. 2018;175:54-59. doi:10.1016/j.solener.2018.01.074
7. Schube J. *Metallization of Silicon Solar Cells With Passivating Contacts*. PhD thesis. Freiburg im Breisgau; 2020.
8. Schube J, Tutsch L, Fellmeth T, et al. Low-resistivity screen-printed contacts on indium tin oxide layers for silicon solar cells with passivating contacts. *IEEE J Photovoltaics*. 2018;8(5):1208-1214. doi:10.1109/JPHOTOV.2018.2859768
9. Oh D, Yousuf H, Dhungel SK, et al. Optimization of the electrode formation mechanism for crystalline silicon heterojunction solar cells. *ECS J Solid State Sci Technol*. 2022;11(9):95002. doi:10.1149/2162-8777/ac8ba5
10. Gensowski K, Jimenez A, Tepner S, et al. Dispensing of low-temperature silver pastes. *AIP Conf Proc*. 2021;2367(1):020007. doi:10.1063/5.0056103
11. Pingel S, Erath D, Wenzel T, et al. Low-temperature Ag-paste screening for silicon heterojunction solar cells and modules. In: *37th European Photovoltaic Solar Energy Conference and Exhibition*; 2020: 508-511. doi:10.4229/EUPVSEC20202020-2DV.3.17
12. Dongpo C, Zhao L, Diao H, Zhang W, Wang G, Wang W. Choice of the low-temperature sintering Ag paste for a-Si:H/c-Si heterojunction solar cell based on characterizing the electrical performance. *J Alloys Compd*. 2015;618:357-365. doi:10.1016/j.jallcom.2014.08.175
13. Erath D, Pospischil M, Keding R, et al. Comparison of innovative metallization approaches for silicon heterojunction solar cells. *Energy Procedia*. 2017;124:869-874. doi:10.1016/j.egypro.2017.09.245
14. Hatt T. *Electroplating Approach Based on Self-Passivated Aluminium Masking for Metallization of Silicon Heterojunction Solar Cells*. PhD thesis. Freiburg im Breisgau; 2021.
15. Erath D, Pingel S, Khotimah R, et al. Fast screen printing and curing process for silicon heterojunction solar cells. *AIP Conf Proc*. 2021; 2367:20006. doi:10.1063/5.0056429
16. Lorenz A, Klawitter M, Linse M, et al. Rotary screen printed metallization of heterojunction solar cells: toward high-throughput production with very low silver laydown. *Energy Tech*. 2022;10(8):2200377. doi:10.1002/ente.202200377
17. Schube J, Fellmeth T, Jahn M, Keding R, Glunz SW. Advanced metallization with low silver consumption for silicon heterojunction solar cells. *AIP Conf Proc*. 2019;2156(1):20007. doi:10.1063/1.5125872
18. Pospischil M, Lorenz A, Kühnhold-Pospischil S, Adrian A. Chapter 7: alternative printing technologies. In: *Silicon Solar Cell Metallization and Module Technology*. 255-307.
19. Gensowski K, Much M, Palme M, et al. Filament stretching during parallel dispensing—a way to reduce silver consumption in SHJ metallization. *Sol Energy Mater Sol Cells*. 2022;245:111871. doi:10.1016/j.solmat.2022.111871
20. Gensowski K, Jimenez A, Freund T, et al. CIGS mini-modules with dispensed metallization on transparent conductive oxide layer. *Sol RRL*. 2020;4(12):2000475. doi:10.1002/solr.202000475
21. Retterstol Olaisen B, Woldegiorgis S, Westin P-O, et al. CIGS mini-modules with screen-printed front contacts. In: *Technical Digest of the 15th International Photovoltaic Science and Engineering Conference*; 2005.
22. Freund T, Zancan N, Kaune G, et al. Large area screen-printed front contact metallization for thin-film solar module production. In: *37th European Photovoltaic Solar Energy Conference and Exhibition*; 2020.
23. Gensowski K, Freund T, Tepner S, Clement F. Increasing the effective area of small-sized CIGS modules by printed ag front contacts. *Phys Status Solidi - Rapid Res Lett*. 2022;16(7):2200040. doi:10.1002/pssr.202200040
24. Petrova-Koch V, Hezel R, Goetzberger A (Eds). *High-Efficient Low-Cost Photovoltaics: Recent Developments*. 2nd ed. Springer-Verlag; 2019. doi:10.1007/978-3-030-22864-4
25. Heske C, Lincot D, Powalla M, Salomé P, Schlatmann R, Tiwari AN, Linden H, Melkonyan K, Petroca-Koch V, Wade A, Dalibor T, Dimmler B, Lundberg O, Petroncini S, Poplavskyy D, Rühle U, Schneider H, Fischer M, Jaremalm E, Reinhardt H. *CIGS White Paper 2019*. 2019. Available at: https://cigs-pv.net/wortpresse/wp-content/uploads/2019/04/CIGS_White_Paper_2019_online.pdf
26. Bermudez V. An overview on electrodeposited Cu (In, Ga)(Se, S)$_2$ thin films for photovoltaic devices. *Sol Energy*. 2018;175:2-8. doi:10.1016/j.solener.2018.03.002
27. Bermudez V. Economical and operational issues for CIGS in the future PV panorama. *Sol Energy*. 2017;146:85-93. doi:10.1016/j.solener.2017.02.023
28. Bermudez V, Perez-Rodriguez A. Understanding the cell-to-module efficiency gap in Cu(In, Ga)(S, Se)$_2$ photovoltaics scale-up. *Nat Energy*. 2018;3(6):466-475. doi:10.1038/s41560-018-0177-1
29. Pingel S, Erath D, Wenzel T, Bivour M, Linse M, Lorenz A, Clement F. *Evaluation of Screen-Printed Ultra-Low-Temperature Metallization for Silicon-Perovskite Tandem Solar Cell*. 2022.
30. Kamino BA, Paviet-Salomon B, Moon S-J, et al. Low-temperature screen-printed metallization for the scale-up of two-terminal perovskite–silicon tandems. *ACS Appl Energy Mater*. 2019;2(5):3815-3821. doi:10.1021/acsaem.9b00502
31. Rehman A, van Kerschaver EP, Aydin E, Raja W, Allen TG, de Wolf S. *Electrode Metallization for Scaled Perovskite/Silicon Tandem Solar Cells: Challenges and Opportunities. Progress in Photovoltaics*; 2021. doi:10.1002/pip.3499
32. Goldstein JI, Joy DC, Michael JR, Ritchie NW, Scott JHJ. *Scanning Electron Microscopy and X-Ray Microanalysis*. 4th ed. Springer; 2018. doi:10.1007/978-1-4939-6676-9
33. Höhne G, Hemminger W, Flammersheim H-J. *Differential Scanning Calorimetry*. 2nd ed. Springer; 2003. doi:10.1007/978-3-662-06710-9
34. Pospischil M. *A Parallel Dispensing System for an Improved Front Surface Metallization of Silicon Solar Cells*. PhD thesis. Freiburg im Breisgau; 2016.
35. Pospischil M, Klawitter M, Kuchler M, et al. High speed dispensing with novel 6 print head. *Energy Procedia*. 2016;98:61-65. doi:10.1016/j.egypro.2016.10.081
36. Pospischil M, Riebe T, Jimenez A, et al. Applications of parallel dispensing in PV metallization. *AIP Conf Proc*. 2019;2156(1):20005. doi:10.1063/1.5125870
37. Gensowski K, Much M, Bujnoch E, Spahn S, Tepner S, Clement F. Filament stretching during micro-extrusion of silver pastes enables an improved fine-line silicon solar cell metallization. *Sci Rep*. 2022;12(1):12318. doi:10.1038/s41598-022-16249-5
38. Tepner S, Wengenmeyr N, Linse M, Lorenz A, Pospischil M, Clement F. The link between Ag-paste rheology and screen-printed solar cell metallization. *Adv Mater Technol*. 2020;5(10):2000654. doi:10.1002/admt.202000654
39. Pospischil M, Klawitter M, Kuchler M, et al. Development of a high-throughput fine line metallization process using CFD-simulation. In: *2013 IEEE 39th Photovoltaic Specialists Conference*. 2250-2253.
40. Verma DD, Fahr A. Confocal laser scanning microscopy. In: *Percutaneous Penetration Enhancers*. CRC Press; 2005:349-372. doi:10.1201/9781420039207.ch23

41. Wenzel T, Lorenz A, Lohmüller E, et al. Progress with screen printed metallization of silicon solar cells—towards 20 µm line width and 20 mg silver laydown for PERC front side contacts. *SSRN*. 2022;244:111804.
42. Takahashi H, Sato A, Takakura M, et al. A new method of surface preparation for high spatial resolution EPMA/SEM with an argon ion beam. *Microchim Acta*. 2006;155(1–2):295-300. doi:10.1007/s00604-006-0559-0
43. Reeves GK, Harrison HB. Obtaining the specific contact resistance from transmission line model measurements. *IEEE Electron Device Lett*. 1982;3(5):111-113. doi:10.1109/EDL.1982.25502
44. Schroder DK. *Semiconductor Material and Device Characterization*. John Wiley & Sons, Inc; 2005. doi:10.1002/0471749095
45. van Humbeeck J. Simultaneous thermal analysis. In: *Handbook of Thermal Analysis and Calorimetry, Principles and Practice*. 497-508.
46. Pospischil M, Specht J, Konig M, et al. Paste rheology correlating with dispensed finger geometry. *IEEE J Photovoltaics*. 2014;4(1):498-503. doi:10.1109/JPHOTOV.2013.2278657
47. Buffat P, Borel JP. Size effect on the melting temperature of gold particles. *Phys Rev A*. 1976;13(6):2287-2298. doi:10.1103/PhysRevA.13.2287
48. Peng P, Hu A, Gerlich AP, Zou G, Liu L, Zhou YN. Joining of silver nanomaterials at low temperatures: processes, properties, and applications. *ACS Appl Mater Interfaces*. 2015;7(23):12597-12618. doi:10.1021/acsami.5b02134
49. Greer JR, Street RA. Thermal cure effects on electrical performance of nanoparticle silver inks. *Acta Mater*. 2007;55(18):6345-6349. doi:10.1016/j.actamat.2007.07.040
50. Pokluda O, Bellehumeur CT, Vlachopoulos J. Modification of Frenkel's model for sintering. *AIChE J*. 1997;43(12):3253-3256. doi:10.1002/aic.690431213
51. Mir H, Arya V, Hoffler H, Brand A. A novel TLM analysis for solar cells. *IEEE J Photovoltaics*. 2019;9(5):1336-1342. doi:10.1109/JPHOTOV.2019.2923337
52. Tutsch L. *Implementing Sputter-Deposited Transparent Conductive Metal Oxides Into Passivating Contacts for Silicon Solar Cells*. PhD thesis. Freiburg im Breisgau; 2020.
53. Luderer C, Tutsch L, Messmer C, Hermle M, Bivour M. Influence of TCO and a-Si:H doping on SHJ contact resistivity. *IEEE J Photovoltaics*. 2021;11(2):329-336. doi:10.1109/JPHOTOV.2021.3051206
54. Jung K-H, Min KD, Lee C-J, et al. Effect of epoxy content in Ag nanoparticle paste on the bonding strength of MLCC packages. *Appl Surf Sci*. 2019;495:143487. doi:10.1016/j.apsusc.2019.07.229

How to cite this article: Gensowski K, Freund T, Much M, Muramatsu K, Tepner S, Clement F. Curing conditions for low-resistivity contacts on transparent conductive oxide layers for different solar cell applications. *Prog Photovolt Res Appl*. 2024; 32(2):102-114. doi:10.1002/pip.3740